

Received 17 March 2026, accepted 23 March 2026, date of publication 25 March 2026, date of current version 30 March 2026.

Digital Object Identifier 10.1109/ACCESS.2026.3677622

RESEARCH ARTICLE

Dynamic Performance of Parallel Heterogeneous Grid-Forming Inverters During Islanding and Grid Resynchronization

ZAHRA AHMADIMONFARED¹ AND STEFAN EICHNER¹

Fraunhofer Institute for Solar Energy Systems—ISE, 79110 Freiburg im Breisgau, Germany

Corresponding author: Zahra Ahmadimonfared (zahra.ahmadimonfared@ise.fraunhofer.de)

ABSTRACT Modern power systems with high inverter penetration face reduced inertia and increased frequency instability during disturbances, necessitating grid-forming inverters (GFMs) that emulate synchronous-machine dynamics. This study examines the parallel operation of a Virtual Synchronous Machine (VSM) controlled and a synchronverter-controlled GFM in a low-inertia microgrid across the full operational cycle of grid-connected, islanded, and resynchronization phases. A unified simulation framework was developed to systematically evaluate the impact of coordinated variations in virtual inertia (H) and damping coefficient (D_p) on frequency dynamics, power sharing, and stability under power imbalance and grid-code-compliant reconnection conditions. The results demonstrate that a higher virtual inertia limits the rate of change of frequency and nadir after islanding, while increased damping enhances oscillation suppression and settling performance. During resynchronization, both GFM satisfy IEEE Std 1547–2018 limits on voltage, frequency, and phase-angle differences, confirming stable interaction and seamless transition between the operating modes. These findings reveal the complementary strengths of heterogeneous VSM–synchronverter operation and the critical role of unified parameter tuning for robust microgrid performance in low-inertia environments

INDEX TERMS Grid-forming inverters, virtual synchronous machine, synchronverter, islanding, grid resynchronization, grid stability.

I. INTRODUCTION

The rapid displacement of synchronous generators by inverter-based renewable energy sources in modern power systems has significantly reduced system inertia, leading to increased rates of change of frequency (RoCoF), larger frequency nadirs, and diminished transient stability during disturbances [2]. Grid-following inverters (GFLs), which rely on phase-locked loops (PLLs) for grid synchronization, cannot provide inherent inertial response comparable to synchronous machines, exhibit degraded performance in weak grids, and are not suited for autonomous islanded operation, thereby motivating the adoption of GFMs. GFMs emulate the inertial response, voltage regulation, and

damping characteristics of synchronous machines, establishing autonomous voltage and frequency references at the point of common coupling (PCC) to support both grid-connected and islanded microgrid operations [3]. Among the various grid-forming control strategies proposed in the literature, synchronverter [4] and Virtual Synchronous Machine (VSM) [5] controls have emerged as particularly attractive options because they reproduce the swing-equation dynamics of synchronous machines through virtual inertia and damping while retaining the flexibility of power electronic interfaces [6].

Synchronverter control preserves the structure of the synchronous generator model, including rotor dynamics and electromagnetic interactions, which facilitates intuitive tuning and enables black-start capability and stable power sharing without communication in microgrids [7].

The associate editor coordinating the review of this manuscript and approving it for publication was Sarasij Das¹.

VSM control, on the other hand, typically combines active and reactive power droop characteristics with tunable virtual inertia and damping coefficients, providing additional freedom to shape the frequency and voltage response during disturbances and in low-inertia grids [8].

In practical applications, multiple grid-forming units are typically required to operate in parallel to supply larger loads, improve redundancy, and enhance reliability in islanded microgrids and weak-grid scenarios. In real microgrid deployments, GFMs with different control implementations may operate simultaneously, which introduces heterogeneous controller interactions that remain insufficiently understood. However, most existing studies examine parallel operation only under homogeneous droop-based grid-forming control, without considering heterogeneous GFM structures such as synchronverter and VSM combinations. For example, Salem et al. [9] investigates a microgrid consisting of two grid-forming inverters, both operating with standard P–f and Q–V droop controllers. The study demonstrates correct active and reactive power sharing under varying load conditions, but both GFMs employ identical droop-based control, and no alternative grid-forming mechanisms or inertia–damping variations are explored. Similarly, Thilekha et al. [10] analyze the dynamic behavior of two parallel GFMs using a detailed dynamic-phasor small-signal model. Their results show how virtual inertia and droop coefficients influence oscillatory modes and post-disturbance stability, yet the work again assumes matching droop/VSM-type controllers on both inverters and does not investigate interactions between fundamentally different grid-forming control laws or operational transitions such as grid reconnection. A related study by Moustafa et al. [11] also considers two droop-controlled GFMs in parallel and proposes an adaptive adjustment of droop coefficients to improve power-sharing accuracy under unequal feeder impedances or different distributed generation (DG) power ratings. While effective for enhancing droop performance, this approach remains constrained to identical droop-based GFMs and does not address heterogeneous controller behavior or full-cycle dynamics. A related contribution is presented in [12], where synchronization and resynchronization of grid-forming inverters are addressed using droop-based V – f control. Although the study focuses on seamless reconnection, it is limited to homogeneous droop-controlled inverters and does not consider heterogeneous grid-forming controllers or parametric variations in virtual inertia and damping. Recent work has also investigated advanced virtual inertia control strategies for improving frequency regulation in renewable-dominated microgrids. For example, Maaruf et al. [13] propose a robust optimal virtual inertia control approach to enhance frequency regulation under high renewable penetration. However, their work focuses on control optimization for frequency support and does not investigate the interaction of heterogeneous grid-forming controllers or system behavior during islanding and grid resynchronization events. A related study is presented in [14], where the stability of a fully inverter-based power

system with multiple heterogeneous grid-forming controllers, including VSM, synchronverter, and droop-controlled units, is investigated. However, that work focuses on system-level stability of heterogeneous GFMs operating simultaneously and does not analyze dynamic behavior during grid resynchronization events, which is addressed in the present study.

Together, these studies provide valuable insights into parallel GFM behavior, but they consistently rely on uniform droop-style control structures and focus primarily on steady-state power sharing or small-signal dynamics. No studies have examined the interaction of heterogeneous GFM controllers such as a synchronverter operating in parallel with a VSM nor do they evaluate the complete operational sequence of grid-connected, islanded, and reconnection phases under systematic variations of virtual inertia and damping. To address this gap, the objective of this study is to investigate the dynamic interaction of heterogeneous grid-forming controllers and their stability during islanding and grid resynchronization. The main contributions of this work are summarized as follows:

- Parallel operation of heterogeneous grid-forming controllers, specifically synchronverter and virtual synchronous machine (VSM) approaches;
- Evaluation of the complete operational cycle, including grid-connected operation, transition to islanded mode, and resynchronization;
- A systematic parametric analysis of virtual inertia H and damping D_p was performed to assess their influence on the system dynamics and stability.

This work addresses the identified gaps through RMS simulations carried out in DIGSILENT PowerFactory 2025, analyzing heterogeneous synchronverter–VSM parallel operation across grid-connected, islanded, and resynchronization phases under systematic variations of virtual inertia H and damping D_p . This study evaluates the frequency dynamics, power sharing behavior, and compliance with IEEE Std 1547–2018 reconnection limits [1] under different phase-angle conditions. These results provide practical tuning guidelines for robust mixed grid-forming microgrid performance in low-inertia power systems.

II. GRID-FORMING INVERTER MODELING AND CONTROL

GFMs are power electronic converters that operate as controllable AC voltage sources, autonomously establishing the voltage magnitude (E), frequency (ω), and phase angle (θ) at their PCC. In contrast to grid-following inverters (GFIs), which rely on PLLs to synchronize with an externally imposed grid voltage, GFMs directly define local voltage and frequency references. This capability enables stable operation in weak grids, islanded microgrids, and low-inertia power systems with a high penetration of inverter-based resources [15].

A typical GFM system consists of a DC energy source, a voltage-source inverter, and an output filter that interfaces the converter with the AC network. Local measurements of voltage and current at the PCC are used to regulate the

active and reactive power exchanged with the grid [16]. The control principle follows the fundamental behavior of synchronous machines: active power is regulated through frequency and phase-angle dynamics, while reactive power is controlled via the voltage magnitude. This inherent decoupling between active power–frequency and reactive power–voltage dynamics enables decentralized and stable power sharing among multiple GFM units without the need for communication.

By actively regulating voltage magnitude and frequency, GFMs can deliver essential grid-support functions such as voltage control, frequency stabilization, and virtual inertia provision. These capabilities allow GFMs to actively participate in system dynamics rather than passively following the grid, making them a key enabling technology for maintaining stability and reliability in modern power systems with a high penetration of inverter-based resources [17].

A. VIRTUAL SYNCHRONOUS MACHINE

The VSM is a GFM control strategy that emulates the electromechanical dynamics of a synchronous generator within an inverter control system. Its primary objective is to provide virtual inertia and damping, which are essential for frequency stability in power systems with a high penetration of inverter-based resources and reduced synchronous generation. By reproducing synchronous-machine-like behavior, the VSM enables inverters to actively contribute to system stability, particularly in low-inertia operating conditions [18]. At the core of the VSM concept is the explicit implementation of the swing equation, which governs the rotational dynamics of the synchronous machines. In this formulation, the active power setpoint P_0 is interpreted as a virtual mechanical input, and the measured active power output P represents the electrical response. The imbalance between these quantities is processed through virtual inertia and frequency-feedback terms, resulting in the following dynamic relationship [19]:

$$J\omega_0 \frac{d \Delta\omega}{dt} = P_0 - P - (K_d + D_p) \Delta\omega, \tag{1}$$

where J denotes the virtual moment of inertia, ω_0 is the nominal angular frequency, and $\Delta\omega = \omega - \omega_0$ represents the frequency deviation with respect to nominal frequency. In this implementation, both K_d (droop-like frequency feedback) and D_p (additional damping) act on $\Delta\omega$, and their combined effect determines the effective damping of the virtual rotor dynamics.

The inverter frequency is reconstructed as

$$\omega = \omega_0 + \Delta\omega, \tag{2}$$

and subsequently integrated to obtain the virtual rotor angle,

$$\dot{\theta} = \omega, \tag{3}$$

where θ is the instantaneous phase angle of the inverter output voltage. This angle reference is used to synthesize the inverter voltage waveform.

Through this control structure, the VSM introduces inertia-like dynamics that can limit the RoCoF during disturbances and improve frequency stability [20]. The combined use of droop-like feedback and damping supports steady-state regulation while providing well-damped transient responses. The dynamic performance of the VSM depends strongly on parameter tuning particularly J and D_p which must be selected to balance the stability and responsiveness across operating conditions. Figure 1 illustrates the VSM control concept, highlighting the implementation of the virtual inertia, damping, and power frequency dynamics.

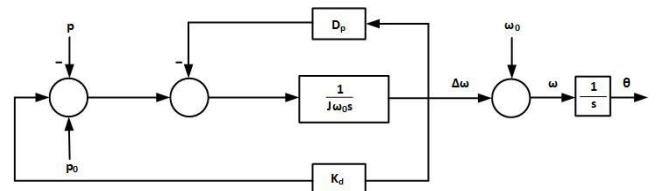


FIGURE 1. Block diagram of VSM control illustrating virtual inertia, damping, and power–frequency dynamics.

B. SYNCHRONVERTER

The synchronverter is a GFM control strategy designed to emulate the dynamic behavior of a synchronous generator with a higher degree of physical fidelity than VSM approaches. Whereas VSM-based methods primarily reproduce swing-equation-like frequency dynamics through virtual inertia and damping, the synchronverter additionally embeds internal electrical machine relations, including electromagnetic torque production and excitation-based voltage regulation. By incorporating the both mechanical and electrical characteristics of synchronous generators into the inverter control structure, the synchronverter enables a more comprehensive emulation of the synchronous machine behavior [7]. The overall control architecture is organized such that active-power dynamics govern the frequency behavior, whereas reactive-power dynamics regulate the voltage magnitude, as illustrated in Fig. 2.

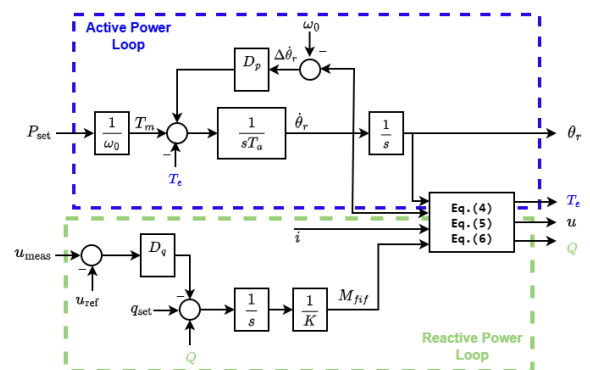


FIGURE 2. Synchronverter control structure with active-power (frequency) and reactive-power (voltage) control loops.

Synchronverter frequency dynamics are commonly expressed in a swing-equation-based form using the virtual angular frequency ω as the state variable. The active-power loop is formulated as: [19]

$$T_a \dot{\omega} = T_m - T_e - D_p(\omega - \omega_0), \quad (4)$$

where T_a is the inertia-related time constant (typically chosen as $T_a = 2H$), D_p is the damping coefficient, ω_0 is the nominal angular frequency, T_m is the mechanical torque reference derived from the active power setpoint, and T_e is the electromagnetic torque produced by the inverter. The virtual rotor angle is then obtained by integration with $\dot{\theta} = \omega$.

where θ defines the instantaneous phase angle used to synthesize the inverter output voltage.

The electromagnetic torque couples the electrical output to the virtual mechanical dynamics and is given by [7]:

$$T_e = M_f i_f \langle \mathbf{i}, \widetilde{\sin}(\theta_r) \rangle, \quad (5)$$

where $\mathbf{i} = [i_a, i_b, i_c]^T$ is the stator current vector, i_f is the excitation current, M_f is the mutual inductance, and θ_r is the rotor electrical angle.

Voltage regulation is achieved through excitation control by adjusting i_f , which modifies the magnitude of the internal electromotive force (EMF). The internal EMF is expressed as follows [7]:

$$\mathbf{u} = \omega M_f i_f \widetilde{\sin}(\theta_r), \quad (6)$$

and the corresponding instantaneous reactive power is given by [7]

$$Q = -\omega M_f i_f \langle \mathbf{i}, \widetilde{\cos}(\theta_r) \rangle. \quad (7)$$

The trigonometric projection vectors used in (5)–(7) are defined as

$$\begin{aligned} \widetilde{\sin}(\theta_r) &= \begin{bmatrix} \sin(\theta_r) \\ \sin\left(\theta_r - \frac{2\pi}{3}\right) \\ \sin\left(\theta_r + \frac{2\pi}{3}\right) \end{bmatrix}, \\ \widetilde{\cos}(\theta_r) &= \begin{bmatrix} \cos(\theta_r) \\ \cos\left(\theta_r - \frac{2\pi}{3}\right) \\ \cos\left(\theta_r + \frac{2\pi}{3}\right) \end{bmatrix}. \end{aligned} \quad (8)$$

Within this formulation, frequency regulation is achieved by balancing the torque reference T_m and the electromagnetic torque T_e through (4), whereas voltage regulation is obtained by controlling the excitation current i_f and the internal EMF in (6). By explicitly modeling inertia-related dynamics, damping, and electrical torque interactions, the synchronverter provides inertia-like frequency support and voltage regulation capabilities, enabling inverter-based resources to closely reproduce the steady-state and transient behaviors of synchronous generators in grid-forming operation [21].

III. SIMULATION FRAMEWORK AND TEST SYSTEM

The proposed study was conducted using the DlgSILENT PowerFactory 2025 in the RMS simulation mode. The investigated system represents a low-inertia microgrid consisting of two grid-forming inverters (VSM and Synchronverter) operating in parallel and connected to the main grid through a controllable switch at the PCC. A schematic of the test system is shown in Fig. 3.

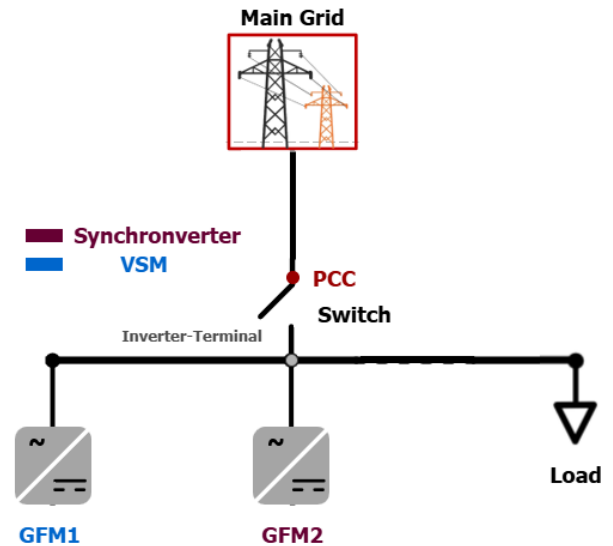


FIGURE 3. Test system with two parallel grid-forming inverters connected to the main grid at the PCC.

The external grid is modeled as a three-phase voltage source with a nominal frequency of 50 Hz and a finite grid impedance, representing a realistic medium-voltage (MV) stiff grid connection. The grid impedance was selected for a 20 kV MV system with an X/R ratio of approximately 10, which is typical for MV networks. The resulting grid parameters are $R_g = 0.6634 \Omega$ and $X_g = 6.6336 \Omega$. Two GFMs, denoted as GFM1 (VSM) and GFM2 (Synchronverter), are connected in parallel at a common inverter terminal bus supplying a constant PQ load. The inverter terminal is electrically separated from the PCC by a circuit breaker (switch) that enables controlled islanding and resynchronization events. Voltage and current measurements were taken at both the inverter terminal and the PCC to capture the local inverter behavior as well as grid-side dynamics.

GFM1 operates under VSM control, whereas GFM2 is implemented using a synchronverter control. Both inverters have identical ratings and operate as grid-forming voltage sources during all simulation phases. The total load connected to the inverter terminal bus was modeled as a constant PQ load, and its parameters are summarized in Table 1. A deliberate active-power deficit is introduced in an islanded operation by setting the combined inverter active-power references below the load demand. This configuration excites the frequency dynamics and enables a clear assessment of

the inertia, damping, and power-sharing behavior of the GFM controllers.

The system initially operated in grid-connected mode. At $t = 59$ s, the circuit breaker at the PCC is opened, disconnecting the main grid and forcing the two GFMs to supply the load during the islanded operation. Grid resynchronization is subsequently performed based on grid-code-compliant conditions, ensuring appropriate adaptation of the voltage magnitude, frequency, and phase angle between the inverter terminal and the PCC prior to reclosing. This approach allows the investigation of inverter dynamics during reconnection without imposing artificial synchronization constraints. Reconnection is permitted only when the voltage magnitude, frequency, and phase-angle differences between the inverter terminal and the PCC satisfy the limits specified in IEEE Std 1547–2018 [1].

A systematic parameter sweep was conducted for both grid-forming controllers by varying the virtual inertia and damping-related parameters while maintaining the same rated power and network conditions. The virtual inertia constant H was swept from 2 to 12 in steps of 2, and the damping coefficient D_p was varied from 150 to 250 in steps of 25. This framework enables a consistent and fair comparison of the VSM and synchronverter performance across grid-connected, islanded, and resynchronization operating modes. The inertia range is consistent with typical synchronous generator inertia constants reported in the literature [19], while D_p is a controller tuning parameter without a fixed standard value.

IV. GRID OPERATING SCENARIOS

A set of representative operating scenarios is defined to analyze the dynamic behavior of two parallel grid-forming inverters under practical grid conditions. The scenarios encompass grid-connected operation, transition to islanded mode, and subsequent grid resynchronization, capturing typical operating events in microgrids and low-inertia power systems. These cases enable an assessment of the coordinated interaction between heterogeneous GFM control strategies at the system level.

Across all scenarios, key grid-forming control parameters namely the virtual inertia H and damping coefficient D_p are varied to examine their impact on frequency dynamics and resynchronization performance. The virtual inertia was set to $H = \{2, 4, 6, 8, 10, 12\}$, while the damping coefficient was varied as $D_p = \{150, 200, 250\}$.

A. GRID-CONNECTED OPERATION

In the initial operating condition, the system operates in the grid-connected mode with both GFMs running in parallel with the external grid. During this phase, the GFMs are assigned identical active power references, resulting in a balanced power injection and stable synchronization at the PCC. The connected PQ load was partially supplied by the GFMs, with the remaining power exchanged with the external grid according to the operating point. This operating

condition establishes a steady-state reference and is used to verify the correct synchronization and baseline power-sharing behavior prior to islanding.

B. ISLANDING SCENARIO

At $t = 59$ s, the circuit breaker at the PCC is opened, disconnecting the external grid and transitioning the system to islanded operation. Following islanding, the two GFMs exclusively supplied the connected load. Because the combined active power references of the GFMs are set below the load demand, an active-power deficit is introduced, leading to a frequency deviation. This scenario is used to evaluate the inertial response, damping behavior, and frequency stability of different grid-forming control strategies under power-deficit conditions.

C. GRID RESYNCHRONIZATION

Following a period of islanded operation, the microgrid was reconnected to the external grid. Resynchronization was performed in accordance with IEEE Std 1547–2018 [1], which defines permissible limits on voltage magnitude, frequency, and phase-angle deviations prior to reconnection. Accordingly, reclosing is permitted only when the differences between the inverter terminal and the PCC satisfy the specified grid-code thresholds.

Due to the dependence of the voltage, frequency, and phase-angle convergence on the selected control parameters and operating conditions, the time required to satisfy the resynchronization criteria varies across the investigated scenarios. This standards-compliant, adaptive resynchronization process mitigates excessive transients and power surges at the instant of reconnection, and enables assessment of the robustness of coordinated GFM operation during this critical transition under practical grid-code constraints.

V. RESULTS AND DISCUSSION

Power-sharing behavior over the full operating sequence.

Figure 4 shows the active power contributions of the VSM-controlled inverter and the synchronverter-controlled inverter over the complete operating sequence, including grid-connected operation, islanding at $t = 59$ s, and grid resynchronization at $t = 133.7$ s.

During the grid-connected operation, both inverters inject their scheduled active power, while the remaining load demand is supplied by the external grid. Following islanding, the synchronverter contributes a larger share of the additional load demand, whereas the VSM maintains an active power close to the reference value. This behavior reflects the selected control tuning, where the torque-based dynamics and effective damping of the synchronverter lead to a more pronounced active power response, whereas the VSM exhibits a comparatively conservative adjustment.

After grid resynchronization, both inverters smoothly returned to their grid-connected operating points without sustained oscillations, confirming stable interaction and

TABLE 1. Grid source and system parameters.

Parameter	Symbol	Value	Unit
Nominal frequency	f_0	50	Hz
Nominal angular frequency	ω_0	$2\pi f_0$	rad/s
Grid representation	–	Voltage source with impedance	N/A
Grid resistance	R_g	0.6634	Ω
Grid reactance	X_g	6.6336	Ω
Rated inverter power (each)	S_{rated}	10	MW
Load type	–	Constant PQ	N/A
Active load power	P_{load}	5	MW
Islanding time	t_{isl}	59	s
Resynchronization strategy	–	Grid-code-based adaptation	N/A

TABLE 2. VSM control parameters (GFM1).

Parameter	Symbol	Value	Unit
Active power setpoint	$P_{set,VSM}$	1.5	MW
Virtual inertia constant	H_{VSM}	tunable between 2 to 12	s
Drop coefficient	$K_{d,VSM}$	10	MW/(rad/s)
Damping coefficient	$D_{p,VSM}$	tunable between 150 to 250	pu

TABLE 3. Synchronverter control parameters (GFM2).

Parameter	Symbol	Value	Unit
Active power setpoint	$P_{set,Syn}$	1.5	MW
Virtual inertia constant	H_{Syn}	tunable between 2 to 12.5	s
Damping coefficient	$D_{p,Syn}$	tunable between 150 to 250	pu
Reactive power gain	k_q	1000	N/A
Reactive power damping gain	D_q	20	N/A

coherent power sharing between the heterogeneous grid-forming controllers throughout the entire operating cycle.

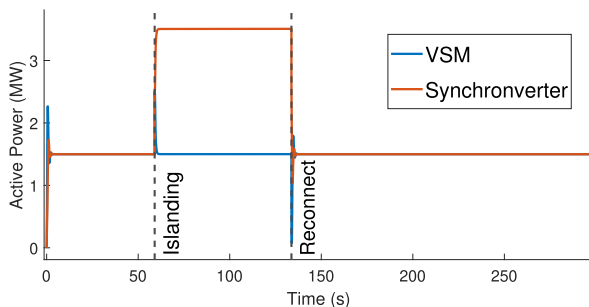


FIGURE 4. Active power of the VSM- and synchronverter-controlled inverters during grid-connected operation, islanding at $t = 59$ s, and grid resynchronization at $t = 133.7$ s.

A. ISLANDING OPERATION UNDER POWER IMBALANCE

At the islanding instant, the circuit breaker at the PCC is opened, electrically separating the microgrid from the external grid and forcing the autonomous operation of the two GFMs. Following the disconnection, the GFMs jointly establish the system voltage and frequency and become solely responsible for supplying the connected load, thereby activating their intrinsic frequency-regulating mechanisms.

The imposed mismatch between scheduled generation and load demand introduces an intentional active power deficit, which constitutes a step disturbance to the system. This disturbance directly excites the frequency dynamics and

reveals the effects of virtual inertia and damping embedded in the GFM controllers. No secondary frequency control or external support was enabled, ensuring that the observed response was governed exclusively by primary grid-forming control loops.

To assess the influence of the control parameters on islanded frequency behavior, two parametric studies were conducted. First, the virtual inertia H was varied from 2 to 12 in steps of 2, while the damping coefficient was fixed at $D_p = 200$, allowing the isolated evaluation of inertial effects on the transient frequency response. Second, the damping coefficient D_p is varied from 150 to 250 in steps of 25 for a fixed value of $H = 10$, in order to assess the role of damping in oscillation attenuation and frequency settling characteristics.

Figure 5 shows the islanded frequency response for different values of virtual inertia. Increasing H leads to a reduced rate of change of frequency immediately after islanding and a smaller maximum frequency deviation, indicating improved short-term frequency stability through inertia emulation.

Figure 6 illustrates the effects of varying the damping coefficient. Higher values of D_p result in stronger damped frequency dynamics and faster convergence toward steady-state operation, whereas lower damping values yield slower settling and more weakly damped responses under the same power imbalance.

Overall, the results confirm that virtual inertia and damping play complementary roles in shaping islanded frequency

dynamics. Appropriate coordination and tuning of H and D_p are therefore essential to achieve stable and well-damped operation in inverter-dominated microgrids subjected to active power imbalance.

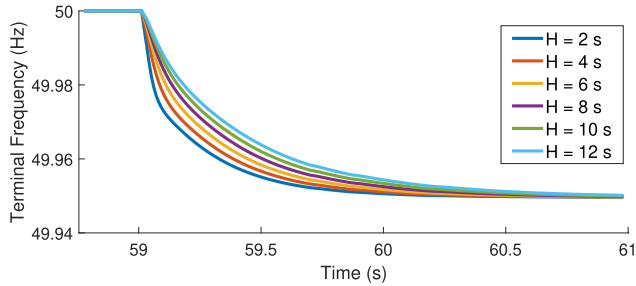


FIGURE 5. Islanded frequency response for different virtual inertia values $H = \{2, 4, 6, 8, 10, 12\}$ with fixed damping $D_p = 200$.

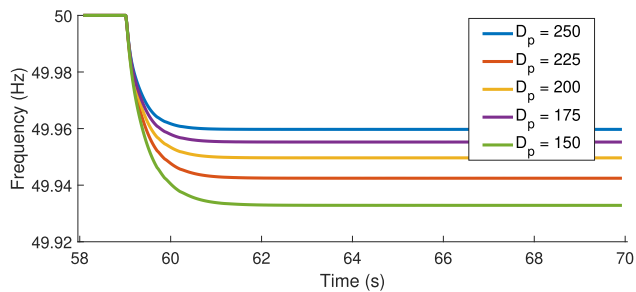


FIGURE 6. Islanded frequency response for different damping coefficients $D_p = \{150, 175, 200, 225, 250\}$ with fixed virtual inertia $H = 10$.

B. GRID RESYNCHRONIZATION REQUIREMENTS AND RECONNECTION LIMITS

Prior to reconnection, inverter-based resources must satisfy synchronization conditions to ensure safe breaker reclosing and avoid excessive transient currents and power surges. In Fig. 3, the *GFM terminal* refers to the locally measured quantities at the inverter terminal (microgrid side), whereas the *PCC* refers to the coupling point to the external grid. Accordingly, synchronization was assessed using the differences between the GFM terminal and PCC in terms of voltage magnitude, frequency, and phase angle.

For the considered setup, the total apparent power rating of the inverter-based resources exceeds 1.5 MVA; therefore, the adopted reconnection limits are ± 0.1 Hz in frequency, $\pm 3\%$ in voltage magnitude, and $\pm 10^\circ$ in phase angle between the GFM terminal and the PCC, in accordance with IEEE Std 1547–2018 [1]. Reconnection is permitted only when all three variables satisfy these limits simultaneously.

Consistent with the islanding analysis, the resynchronization assessment was performed under the same parametric variations of the virtual inertia and damping. For each parameter set, reconnection is evaluated under two representative phase-angle conditions: (i) near-synchronous reconnection, where the phase-angle difference between the GFM terminal and the PCC is close to zero, and (ii) a conservative condition where the phase-angle difference approaches the grid-code

limit of 10° . Since the frequency and phase angle evolve dynamically after islanding as a consequence of the active power imbalance and the selected controller parameters, the time required to satisfy the reconnection limits is not fixed. Therefore, the breaker closing instant is therefore determined adaptively based on the first time at which all synchronization variables lie within their admissible bands for the required duration.

To provide a conservative verification of the limit compliance, the reconnection constraints are illustrated for the most critical settings identified in the parameter sweeps. For the inertia variation, the most demanding case corresponds to the minimum inertia $H = 2$ s with $D_p = 200$ fixed. For the damping variation, the most demanding case corresponds to the minimum damping $D_p = 150$ with $H = 10$ s fixed. Figures 7–9 and Figs. 10–12 show representative PCC and GFM-terminal traces together with the admissible bands, confirming that reconnection is executed only after the limits are satisfied.

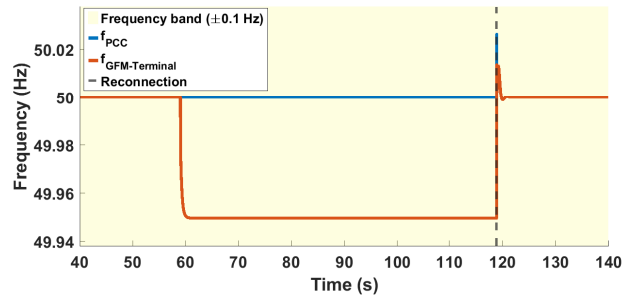


FIGURE 7. Most critical case for the inertia sweep ($H = 2$ s, $D_p = 200$): PCC and grid-forming terminal frequency with the admissible reconnection band ± 0.1 Hz.

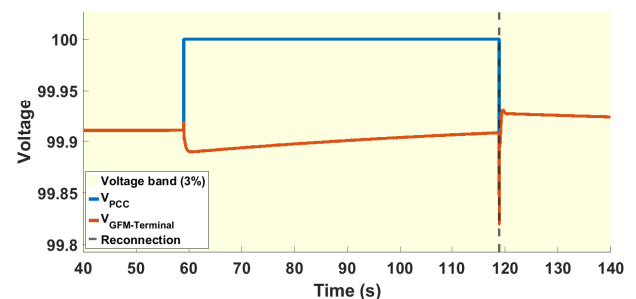


FIGURE 8. Most critical case for the inertia sweep ($H = 2$ s, $D_p = 200$): PCC and grid-forming terminal voltage with the admissible reconnection band $\pm 3\%$.

C. GRID RESYNCHRONIZATION PERFORMANCE UNDER PHASE-ANGLE CONSTRAINTS

After the islanded operation, grid resynchronization is performed by reconnecting the microgrid to the external grid once all synchronization requirements for the voltage magnitude, frequency, and phase angle are simultaneously satisfied. According to IEEE Std 1547–2018 [1], the breaker

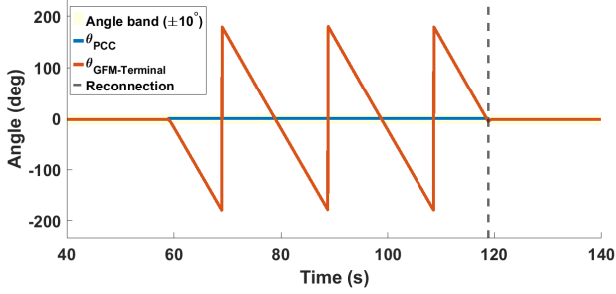


FIGURE 9. Most critical case for the inertia sweep ($H = 2$ s, $D_p = 200$): PCC and grid-forming terminal phase angle with the admissible reconnection band $\pm 10^\circ$.

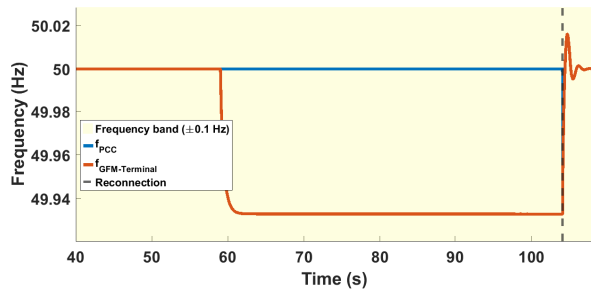


FIGURE 10. Most critical case for the damping sweep ($H = 10$ s, $D_p = 150$): PCC and grid-forming terminal frequency with the admissible reconnection band ± 0.1 Hz.

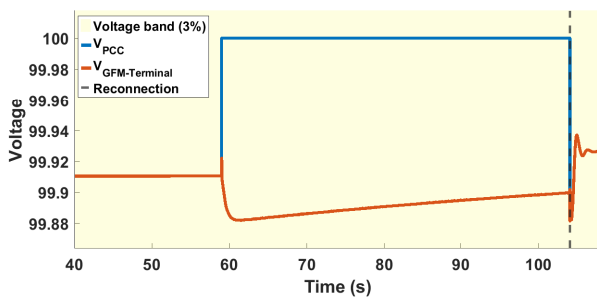


FIGURE 11. Most critical case for the damping sweep ($H = 10$ s, $D_p = 150$): PCC and grid-forming terminal voltage with the admissible reconnection band $\pm 3\%$.

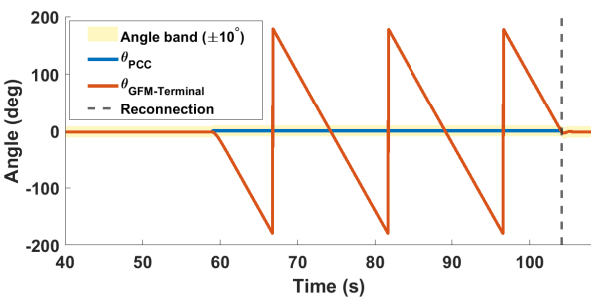


FIGURE 12. Most critical case for the damping sweep ($H = 10$ s, $D_p = 150$): PCC and grid-forming terminal phase angle with the admissible reconnection band $\pm 10^\circ$.

at the PCC is allowed to close only when the corresponding deviations remain within the prescribed admissible limits.

To investigate the sensitivity of resynchronization dynamics to phase-angle alignment, two representative reconnection conditions were considered based on the phase-angle difference between the grid-forming terminal and the PCC at the instant of breaker closure. The **first condition** corresponds to a near-synchronous reconnection, where the phase-angle difference is close to zero. The **second condition** represents a limiting grid-code-compliant case, in which the phase-angle difference approaches the maximum admissible threshold of approximately 10° . These two cases bound the practical range of resynchronization events allowed by the grid code.

Unless otherwise stated, a comparative analysis was performed for a fixed controller configuration with virtual inertia $H = 10$ and damping coefficient $D_p = 250$, corresponding to a well-damped and practically relevant tuning. The resynchronization response was evaluated using the PCC-measured frequency, voltage deviation, and active power, all plotted with respect to the relative time axis

$$\tau = t - t_{rec},$$

where t_{rec} denotes the instant of circuit-breaker closure at the PCC.

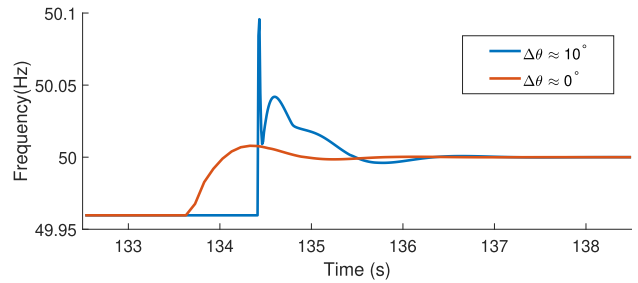


FIGURE 13. PCC frequency during grid resynchronization for near-synchronous ($\Delta\theta \approx 0^\circ$) and limiting ($\Delta\theta \approx 10^\circ$) phase-angle conditions with $H = 10$ and $D_p = 250$, plotted versus the relative time axis $\tau = t - t_{rec}$.

Figure 13 compares the PCC frequency response during grid resynchronization for the near-synchronous ($\Delta\theta \approx 0^\circ$) and limiting ($\Delta\theta \approx 10^\circ$) phase-angle conditions. For the near-synchronous case, the small phase-angle mismatch at the breaker closure resulted in a smooth frequency transition with a limited overshoot and a gradual return to the nominal value. In contrast, the limiting phase-angle case exhibits a sharper frequency excursion immediately after reconnection, characterized by a higher initial peak due to the larger angular mismatch between the microgrid and the external grid. Despite this more pronounced transient, the frequency remained stable and converged to steady state without sustained oscillations, confirming robust resynchronization under grid-code-compliant phase-angle limits. The corresponding PCC voltage deviations and active power exchanges are shown in Figs. 14 and 15, respectively. For the near-synchronous case ($\Delta\theta \approx 0^\circ$), the small phase-angle mismatch at the breaker closure results in a mild voltage dip and a moderate, smoothly varying active power

transient that settles gradually. In contrast, the limiting phase-angle case ($\Delta\theta \approx 10^\circ$) produces a deeper instantaneous voltage deviation and a larger active power surge immediately after reconnection, driven by the higher angular mismatch between the microgrid and the external grid. Despite these more pronounced transients, both voltage and active power responses are well damped and converge to steady state without sustained oscillations, confirming stable operation under grid-code-compliant resynchronization conditions.

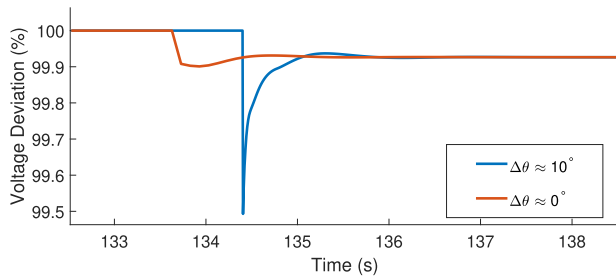


FIGURE 14. PCC voltage deviation during grid resynchronization for near-synchronous and limiting phase-angle conditions with $H = 10$ and $D_p = 250$, plotted versus the relative time axis $\tau = t - t_{rec}$.

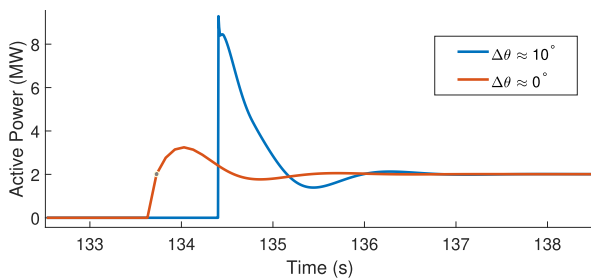


FIGURE 15. PCC active power during grid resynchronization for near-synchronous and limiting phase-angle conditions with $H = 10$ and $D_p = 250$, plotted versus the relative time axis $\tau = t - t_{rec}$.

D. RESYNCHRONIZATION SENSITIVITY TO CONTROL PARAMETER VARIATIONS

To further examine the influence of GFM control parameters during resynchronization, additional simulations are performed by systematically varying the virtual inertia H and the damping coefficient D_p , while ensuring that all synchronization constraints on voltage, frequency, and phase angle remain satisfied at the instant of breaker closure.

1) NEAR-SYNCHRONOUS RESYNCHRONIZATION ($\Delta\theta \approx 0^\circ$)

Effect of virtual inertia. For the near-synchronous phase-angle condition, the effect of virtual inertia is illustrated through the PCC frequency responses shown in Fig. 16. The virtual inertia H was varied while keeping the damping coefficient $D_p = 200$ fixed. Increasing H results in a smoother frequency evolution immediately after reconnection, reducing the rate of change of the frequency and attenuating the initial transient. This behavior reflects the

enhanced inertial buffering provided by higher virtual inertia during the resynchronization process.

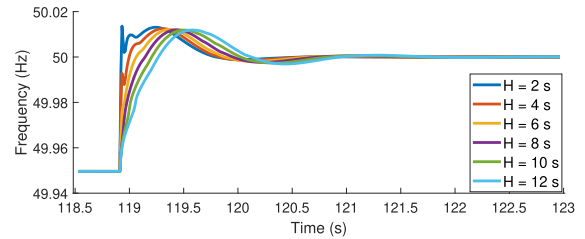


FIGURE 16. PCC frequency during resynchronization for different virtual inertia values H with fixed $D_p = 200$.

Effect of damping. The influence of damping is illustrated in Fig. 17, where the damping coefficient D_p is varied while the virtual inertia is held constant at $H = 10$. In addition to shaping the post-reconnection transient, D_p also affects the time required to satisfy the grid-code synchronization limits and thus the breaker closing instant. This can be understood from the phase–frequency relationship [22]:

$$\frac{d \Delta\theta}{dt} = \Delta\omega(t), \tag{9}$$

where $\Delta\theta(t) = \theta_{GFM}(t) - \theta_{PCC}(t)$ is the phase-angle difference between the GFM terminal and PCC, and $\Delta\omega(t) = \omega_{GFM}(t) - \omega_{grid}(t)$ is the angular frequency difference between the microgrid and external grid. A swing-equation-based approximation of the frequency loop with damping is [23]

$$\frac{2H}{\omega_0} \frac{d \Delta\omega}{dt} = \Delta P - D_p \Delta\omega, \tag{10}$$

where H is the virtual inertia constant, ω_0 is the nominal angular frequency, ΔP denotes the effective active-power imbalance that drives the frequency dynamics, and D_p is the damping coefficient. For a quasi-constant ΔP , the steady-state frequency deviation was

$$\Delta\omega_\infty = \frac{\Delta P}{D_p}, \tag{11}$$

which implies that larger D_p reduces the magnitude of $|\Delta\omega|$ available to drive phase-angle evolution. If phase alignment is achieved predominantly through natural phase drift, an approximate time to reach a target phase-angle change $\Delta\theta^*$ is

$$t_{sync} \approx \frac{\Delta\theta^*}{|\Delta\omega_\infty|} = \frac{\Delta\theta^* D_p}{|\Delta P|}, \tag{12}$$

indicating that increasing D_p can increase the time required to bring $\Delta\theta$ into the admissible window.

For the near-zero phase-angle condition considered in Fig. 17, the extracted reconnection instants increase in an approximately linear manner with the damping coefficient over the investigated range $D_p = 150 - 250$, as summarized in Table 4. The reported percentages indicate the relative

delay in the reconnection time with respect to the baseline case $D_p = 150$.

Consistent with these observations, the lower damping values in Fig. 17 lead to earlier reconnection but a more pronounced frequency overshoot after breaker closure, whereas higher damping values delay reconnection while reducing overshoot and improving transient smoothness. Overall, D_p governs both the resynchronization timing and the severity of post-reconnection transients; therefore, it must be selected to balance fast reconnection against acceptable frequency excursions and well-damped dynamics.

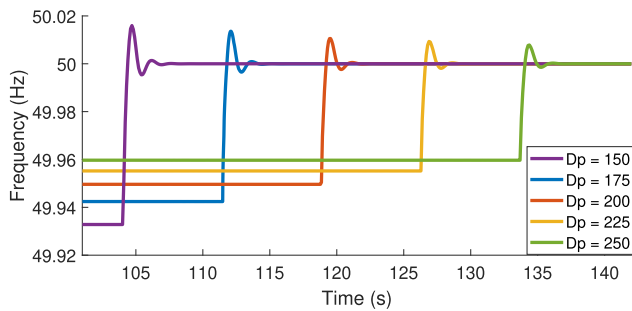


FIGURE 17. PCC frequency during grid resynchronization for different damping coefficients D_p with fixed $H = 10$, plotted versus the relative time axis $\tau = t - t_{rec}$.

TABLE 4. Near-zero phase-angle resynchronization ($H = 10$): reconnection instant for different damping coefficients D_p . The percentage indicates the relative delay in reconnection time with respect to the baseline case $D_p = 150$.

D_p	t_{rec} (s)	Increase (%)
150	104.06	0
175	111.16	7.1
200	118.26	14.2
225	125.50	21.4
250	132.73	28.5

2) LIMITING PHASE-ANGLE RESYNCHRONIZATION

($\Delta\theta \approx 10^\circ$)

For the limiting phase-angle condition, resynchronization occurred when the phase-angle difference between the GFM terminal and PCC approached the maximum admissible grid-code threshold. This condition represents a stressed but still grid-code-compliant reconnection scenario and therefore provides a conservative assessment of the resynchronization performance.

Effect of virtual inertia. The influence of virtual inertia under the same limiting phase-angle condition is shown in Fig. 18. Increasing virtual inertia H reduces the severity of the initial frequency excursion immediately after breaker closure by providing stronger inertial buffering. An analysis was performed for a fixed damping coefficient of $D_p = 200$. Higher inertia values result in a smoother frequency trajectory during the first instants following reconnection, whereas the steady-state frequency convergence remains unaffected. This

behavior confirms that virtual inertia primarily shapes the short-term transient response during stress resynchronization.

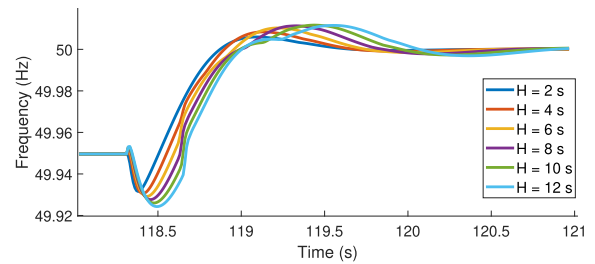


FIGURE 18. PCC frequency during grid resynchronization for different virtual inertia values H under the limiting phase-angle condition ($D_p = 200$), plotted versus the relative time axis $\tau = t - t_{rec}$.

Effect of damping. Under the limiting phase-angle condition, the impact of damping variation is quantified using the peak and nadir frequency metrics extracted from the PCC frequency response. The results are summarized in Table 5. Increasing D_p shifts the frequency peak to later instants, reflecting a slower frequency evolution with higher damping. The nadir frequency improved monotonically as D_p increased, indicating a reduced undershoot. In contrast, the peak frequency is minimized at $D_p = 200$ and did not decrease monotonically for larger D_p . Overall, higher damping delays the dynamics and improves the nadir, while the overshoot reduction exhibits an optimal range of approximately $D_p = 200$ for this case.

TABLE 5. Limiting phase-angle resynchronization: extracted peak and nadir PCC frequency for different damping coefficients D_p with fixed $H = 10$.

D_p	f_{max} (Hz)	$t(f_{max})$ (s)	f_{min} (Hz)
150	50.087	104.55	49.933
175	50.071	111.97	49.942
200	50.050	119.64	49.950
225	50.078	126.93	49.955
250	50.083	134.43	49.960

VI. CONCLUSION

The results show that the stable operation of heterogeneous grid-forming inverters can be achieved across both islanded operation and grid resynchronization through appropriate tuning of virtual inertia and damping. During islanding under active power imbalance, virtual inertia primarily limits the rate of change of frequency and the initial frequency deviation, while damping improves oscillation attenuation and influences the depth of the frequency drop and steady-state convergence, with coherent power sharing observed between the VSM and synchronverter. During grid resynchronization, compliant reconnection is obtained under both near-synchronous ($\Delta\theta \approx 0^\circ$) and limiting ($\Delta\theta \approx 10^\circ$) phase-angle conditions; near-synchronous reconnection leads to mild transients, whereas reconnection close to the admissible phase-angle limit produces stronger but well-damped frequency, voltage, and power excursions. A key

finding is that the damping coefficient not only reduces post-reconnection overshoot but also governs the resynchronization timing by slowing phase-angle convergence, thereby revealing a fundamental trade-off between fast reconnection and transient smoothness. These findings provide practical guidance for coordinated tuning of inertia and damping in low-inertia microgrids with mixed grid-forming control strategies. In addition, the results confirm that heterogeneous grid-forming controllers do not require identical control structures or parameter sets to achieve stable and coherent operation. The combined VSM–synchronverter configuration demonstrates robust interaction across all operating stages, indicating that mixed grid-forming strategies can be effectively deployed in practical microgrids. By explicitly linking islanding and resynchronization behavior through a unified parameter study, this work provides a consistent framework for evaluating and tuning grid-forming inverters under realistic operating constraints. Future work will focus on experimental or hardware-in-the-loop validation of the heterogeneous grid-forming configuration, as well as further investigation of controller interaction under different grid strengths and operating conditions to support practical deployment in inverter-dominated power systems.

REFERENCES

- [1] D. G. Photovoltaics and E. Storage, *IEEE Standard for Interconnection and Interoperability of Distributed Energy Resources With Associated Electric Power Systems Interfaces*, IEEE Standard 1547-2018, Apr. 2018.
- [2] S. Saha, M. I. Saleem, and T. K. Roy, "Impact of high penetration of renewable energy sources on grid frequency behaviour," *Int. J. Electr. Power Energy Syst.*, vol. 145, Feb. 2023, Art. no. 108701.
- [3] S. Anttila, J. S. Döhler, J. G. Oliveira, and C. Boström, "Grid forming inverters: A review of the state of the art of key elements for microgrid operation," *Energies*, vol. 15, no. 15, p. 5517, Jul. 2022.
- [4] M. J. Quintero-Durán, J. E. Candelo-Becerra, M. E. González-Niño, S. A. Hernández-Moreno, and R. F. Váz, "Synchronverter control strategy: A review of different improvements and applications," *Energies*, vol. 18, no. 13, p. 3574, Jul. 2025.
- [5] N. Baeckeland, D. Chatterjee, M. Lu, B. Johnson, and G.-S. Seo, "Overcurrent limiting in grid-forming inverters: A comprehensive review and discussion," *IEEE Trans. Power Electron.*, vol. 39, no. 11, pp. 14493–14517, Nov. 2024.
- [6] N. Mohammed, H. Udawatte, W. Zhou, D. J. Hill, and B. Bahrani, "Grid-forming inverters: A comparative study of different control strategies in frequency and time domains," *IEEE Open J. Ind. Electron. Soc.*, vol. 5, pp. 185–214, 2024.
- [7] Q.-C. Zhong and G. Weiss, "Synchronverters: Inverters that mimic synchronous generators," *IEEE Trans. Ind. Electron.*, vol. 58, no. 4, pp. 1259–1267, Apr. 2011.
- [8] P. Arévalo, C. Ramos, and A. Rocha, "A systematic review of grid-forming control techniques for modern power systems and microgrids," *Energies*, vol. 18, no. 14, p. 3888, Jul. 2025.
- [9] Q. Salem, R. Aljarrah, M. Karimi, and A. Al-Quraan, "Grid-forming inverter control for power sharing in microgrids based on P/f and Q/V droop characteristics," *Sustainability*, vol. 15, no. 15, p. 11712, Jul. 2023.
- [10] T. Thilekha, S. Filizadeh, U. D. Annakkage, C. Karawita, and D. Muthumuni, "Analysis of interactions among parallel grid-forming inverters," *Electric Power Syst. Res.*, vol. 223, Oct. 2023, Art. no. 109652.
- [11] S. H. Moustafa, A. M. Ibrahim, R. A. Taha, A. S. Soliman, M. M. Amin, F. F. El-Sousy, and O. A. Mohammed, "Adaptive power sharing strategies of parallel droop-controlled GFM inverters in AC microgrids," in *Proc. IEEE Ind. Appl. Soc. Annu. Meeting (IAS)*, Jun. 2025, pp. 1–6.
- [12] D. Sharma, F. Sadeque, and B. Mirafzal, "Synchronization of inverters in grid forming mode," *IEEE Access*, vol. 10, pp. 41341–41351, 2022.
- [13] M. Maaruf, S. E. Ferik, F. Saleh Al-Ismael, and M. Khalid, "Robust optimal virtual inertia control for microgrid frequency regulation considering high renewable energy penetration," in *Proc. 11th Int. Conf. Renew. Energy Res. Appl. (ICRERA)*, Sep. 2022, pp. 369–373.
- [14] Z. Ahmadi Monfared and S. Eichner, "Stability assessment of fully inverter-based power systems using grid-forming controls," *Electronics*, vol. 14, no. 21, p. 4202, Oct. 2025.
- [15] R. H. Lasseter, Z. Chen, and D. Pattabiraman, "Grid-forming inverters: A critical asset for the power grid," *IEEE J. Emerg. Sel. Topics Power Electron.*, vol. 8, no. 2, pp. 925–935, Jun. 2020.
- [16] H. Pishbahar, F. Blaabjerg, and H. Saboori, "Emerging grid-forming power converters for renewable energy and storage resources integration—A review," *Sustain. Energy Technol. Assessments*, vol. 60, Dec. 2023, Art. no. 103538.
- [17] K. Rahman, J. Hashimoto, D. Orihara, T. S. Ustun, K. Otani, H. Kikusato, and Y. Kodama, "Reviewing control paradigms and emerging trends of grid-forming inverters—A comparative study," *Energies*, vol. 17, no. 10, p. 2400, May 2024.
- [18] M. Shadoul, R. Ahshan, R. S. Alabri, A. Al-Badi, M. Albadi, and M. Jamil, "A comprehensive review on a virtual-synchronous generator: Topologies, control orders and techniques, energy storages, and applications," *Energies*, vol. 15, no. 22, p. 8406, Nov. 2022.
- [19] P. Kundur, "Power system stability," *Power Syst. Stability Control*, vol. 10, no. 1, pp. 1–7, 2007.
- [20] S. D'Arco and J. A. Suul, "Virtual synchronous machines—Classification of implementations and analysis of equivalence to droop controllers for microgrids," in *Proc. IEEE Grenoble Conf.*, Jun. 2013, pp. 1–7.
- [21] D. B. Rathnayake, M. Akrami, C. Phurailatpam, S. P. Me, S. Hadavi, G. Jayasinghe, S. Zabihi, and B. Bahrani, "Grid forming inverter modeling, control, and applications," *IEEE Access*, vol. 9, pp. 114781–114807, 2021.
- [22] J. Machowski, J. W. Bialek, J. Bialek, and J. R. Bumby, *Power System Dynamics and Stability*. Hoboken, NJ, USA: Wiley, 1997.
- [23] L. L. Grigsby, *Power System Stability and Control*. Boca Raton, FL, USA: CRC Press, 2007.



ZAHRA AHMADIMONFARED was born in Mashhad, Iran, in 1994. She received the M.Sc. degree in electrical engineering, majoring in energy systems planning and management from Azad University, Mashhad Branch, Mashhad, Iran, in 2020. She is currently pursuing the joint Ph.D. degree in photovoltaic engineering with the Distributed Generation and Grid Connection Curriculum, University of Genoa, and the University of Salerno, Italy.

Since 2024, her research has been conducted at Fraunhofer Institute for Solar Energy Systems—ISE, Freiburg im Breisgau, Germany. Her research interests include grid-forming and grid-following inverter control and the stability of inverter-dominated power systems in weak grids.



STEFAN EICHNER was born in Augsburg, Germany, in 1991. He received the B.Sc. degree in energy technology and the M.Sc. degree in electrical engineering from the Friedrich-Alexander-Universität Erlangen-Nürnberg (FAU), Erlangen, Germany, in 2016 and 2019, respectively. Since 2019, he has been a Research Associate with the Fraunhofer Institute for Solar Energy Systems—ISE, Freiburg im Breisgau, Germany. His research interest includes the integration of renewable energy into the power grid and its impact on system stability. Additionally, his work focuses on reactive power management and grid protection strategies.

• • •